The role of symmetry-breaking strains on quartz inclusions in anisotropic hosts: Implications for Raman elastic geobarometry

LITHOS xxx (xxxx) 106716

Contents lists available at ScienceDirect

LITHOS

journal homepage: www.elsevier.com/locate/lithos

The role of symmetry-breaking strains on quartz inclusions in anisotropic hosts: Implications for Raman elastic geobarometry

M. Murri [a,*], J.P. Gonzalez [b], M.L. Mazzucchelli [c,d], M. Prencipe [e], B. Mihailova [f], R.J. Angel [g], M. Alvaro [b]

[a] Department of Earth and Environmental Sciences, University of Milano-Bicocca, Piazza della Scienza 4, I-20126 Milano, Italy
[b] Department of Earth and Environmental Sciences, University of Pavia, Via A. Ferrata 1, 27100 Pavia, Italy
[c] Mainz Institute of Multiscale Modeling, Johannes-Gutenberg University of Mainz, Staudingerweg 7, Mainz 55128, Germany
[d] Institute of Geosciences, Johannes-Gutenberg University of Mainz, J.-J.-Becher-Weg 21, Mainz 55128, Germany
[e] Earth Science Department, University of Torino, Via Valperga Caluso 35, I-10125 Torino, Italy
[f] Department of Earth Sciences, University of Hamburg, Grindelallee 48, D-20146 Hamburg, Germany
[g] Istituto di Geoscienze e Georisorse, CNR, Via Giovanni Gradenigo 6, 35131 Padova, Italy

ARTICLE INFO

Keywords:
Symmetry-breaking strains
Quartz
Host-inclusion system
Ab initio HF/DFT
Raman elastic geobarometry

ABSTRACT

Raman elastic geobarometry for mineral host-inclusion systems is used to determine the strains acting on an inclusion still entrapped in its host by measuring its Raman wavenumber shifts which are interpreted through the phonon-mode Grüneisen tensors of the inclusion phase. The calculated inclusion strains can then be used in an elastic model to calculate the pressure and temperature conditions of entrapment. This method is applied frequently to host inclusion systems where the host is almost elastically isotropic (e.g. garnet) and the inclusion is elastically anisotropic (e.g. quartz and zircon). In this case, when the entrapment occurs under hydrostatic conditions the host will impose isotropic strains on the inclusion which in turn will develop non-hydrostatic stress. In this scenario the symmetry of the inclusion mineral is preserved and the strains in the inclusion can be measured via Raman spectroscopy using the phonon-mode Grüneisen tensor approach.

However, a more complex situation arises when the host-inclusion system is fully anisotropic, such as when a quartz inclusion is entrapped within a zircon host, because the symmetry of the inclusion can be broken due to the external anisotropic strain field imposed on the inclusion by the host, which in turn will modify the phonon modes. We therefore calculated the strain states of quartz inclusions entrapped in zircon hosts in multiple orientations and at various geologically relevant pressure and temperature conditions. We then performed ab initio Hartree-Fock/Density Functional Theory (HF/DFT) simulations on α-quartz in these strain states. These HF/DFT simulations show that the changes in the positions of the Raman modes produced by strains that are expected for symmetry broken quartz inclusions in zircon are generally similar to those that would be seen if the quartz inclusions remained truly trigonal in symmetry. Therefore, the use of the trigonal phonon-mode Grüneisen tensor to determine the inclusion strains does not lead to geologically significant errors in calculated quartz inclusion entrapment pressures in zircon.

1. Introduction

The study and measurement of elastic strains in mineral inclusions has undergone rapid development as a tool to determine the pressure and temperature conditions of inclusion entrapment, thereby providing constraints on the pressure-temperature (i.e. P-T) history of their host minerals and rocks. The strain and stress fields in a crystal are the result of both the surrounding environment (i.e. the hydrostatic or non-hydrostatic stress applied to it) and the elastic properties of the crystal itself. For example, when a crystal is immersed in a liquid medium it will be under hydrostatic pressure and the crystal (e.g. inclusion) will develop isotropic or anisotropic strains depending on its symmetry and its elastic properties (Fig. 1a). However, if the crystal (inclusion) is entrapped within another solid material (i.e. the host) it will be subjected to strains imposed upon it arising from the elastic properties of the host material and the external stress conditions. In our discussion we will as-

* Corresponding author.
E-mail address: mara.murri@unimib.it (M. Murri).

https://doi.org/10.1016/j.lithos.2022.106716
Received 20 October 2021; Received in revised form 6 April 2022; Accepted 22 April 2022
0024-4937/

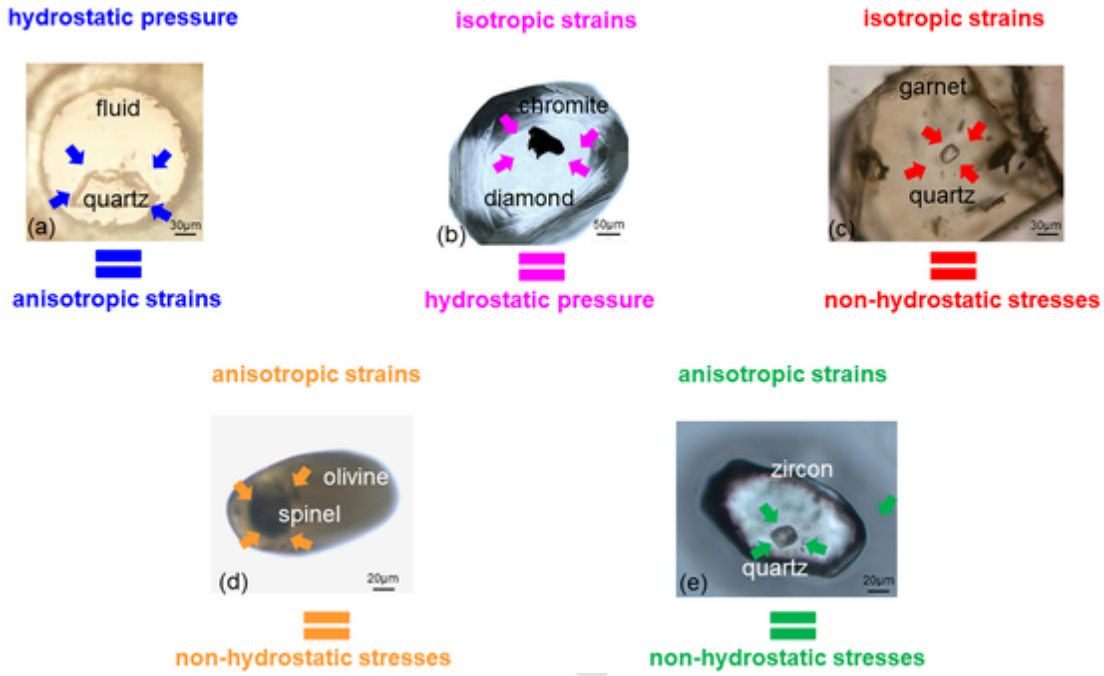

Fig. 1. Illustration of stress and strain states. (a) In a diamond-anvil cell a crystal is immersed in a fluid and is under hydrostatic pressure; (b) An isotropic inclusion in an isotropic host is subject to isotropic strains and it will develop hydrostatic pressure; (c) An anisotropic inclusion in a cubic garnet host is subject to isotropic strain and therefore is under non-hydrostatic stress; (d)An isotropic inclusion in an anisotropic host is subject to anisotropic strains and it will develop non-hydrostatic stresses (e) an anisotropic inclusion in a zircon host is subject to anisotropic strains and therefore is under non-hydrostatic stress whose magnitude depends upon their relative crystallographic orientations.Cases (b-e) assume that the stress acting on the host is hydrostatic.

sume that the external stress on the host is homogenous and hydrostatic. Under this assumption, we can consider four representative cases where the inclusion is spherical and embedded in an infinite host and therefore the stress state of the inclusion is homogeneous and results from the combination of the symmetries and properties of the host and inclusion crystals:

(i) a completely isotropic (or almost isotropic) host-inclusion system such as chromite in diamond (Fig. 1b). In this case, the host mineral will impose an isotropic strain on the entrapped mineral inclusion which in turn will develop an isotropic stress field. It will therefore be under hydrostatic pressure and will remain cubic.
(ii) an isotropic host and an anisotropic inclusion such as quartz in garnet (Fig. 1c). Also in this case the host imposes isotropic strains on the inclusion, but the inclusion being anisotropic will develop a non-hydrostatic stress field but will retain its symmetry.
(iii) an anisotropic host and an isotropic inclusion such as spinel in olivine (Fig. 1d). The elastically anisotropic host will apply anisotropic strains to the elastically isotropic inclusion which will therefore develop a non-hydrostatic stress. The applied anisotropic strain lowers the symmetry of the inclusion.
(iv) a completely anisotropic host-inclusion system such as quartz in zircon (Fig. 1e). In this last case we have the most complex situation considered here: the host is anisotropic and therefore imposes anisotropic strains on the inclusion which, being anisotropic, develops a stress field that depends upon its orientation with respect to the host mineral and the contrast in their elastic properties. These anisotropic strains can lower the symmetry of the inclusion.In addition to these considerations, we note that if the external stress conditions are non-hydrostatic, the stress developed by the inclusion can be non-hydrostatic also when the host is elastically isotropic. More complex situations arise when the stress and the strain in the inclusion are inhomogeneous due to inhomogeneities in the external stress acting on the host or because of geometrical features (morphology of the inclusion, its proximity to other inclusions, or to the external surface of the host, e.g. Mazzucchelli et al., 2018; Zhong et al., 2019).

Mineral inclusions are common in metamorphic rocks and the determination of their apparent entrapment conditions using Raman elastic geobarometry can provide new P-T constraints to understand the metamorphic history of the rock and the geological processes involved (e.g. Alvaro et al., 2020; Rosenfeld and Chase, 1961). Raman elastic geobarometry relies on the joint application of the phonon-mode Grüneisen tensor together with elastic geobarometry theory (e.g. Angel et al., 2019; Murri et al., 2018; Murri et al., 2019). The phonon-mode Grüneisen tensor is a well-established concept (Cantrell, 1980; Grüneisen, 1926; Key, 1967) that relates the shifts of phonon frequencies of a crystal to the strains imposed on a crystal. Being a second-rank symmetric property tensor (Ziman, 1960) that relates to the strain, the Grüneisen tensors are subject to the symmetry of the crystal, not to the symmetries of the individual phonon modes themselves (Angel et al., 2019; Ziman, 1960). While the symmetry constraints on the Grüneisen tensors of all of the modes in a crystal are therefore the same, the values of their components differ and must be determined by experiment (Barron et al., 1982; Briggs and Ramdas, 1977; Cantrell, 1980; Key, 1967) or DFT simulations. Once the values of the components for the Raman active modes have been determined in these ways, this allows us to determine the residual strain state on the inclusions by measuring their Raman wavenumber shifts (e.g. Angel et al., 2019; Murri et al., 2019; Musiyachenko et al., 2021; Stangarone et al., 2019). The strain state of the inclusion can then be used to calculate the apparent entrapment conditions of the host-inclusion system. This method has been largely applied to zircon and quartz inclusions contained in garnet (e.g. Alvaro et al., 2020; Baldwin et al., 2021; Campomenosi et al., 2021; Cisneros et al., 2021; Gilio et al., 2021; Gonzalez et al., 2019; Harvey et al., 2020; Johnson et al., 2020; Schrojenstein Lantman et al., 2021;

Zhong et al., 2019), in which cases the symmetry of the inclusion is preserved, since the strain applied to it is isotropic (see case ii above and Fig. 1c). Moreover, when an anisotropic inclusion is spherical and isolated within an isotropic host mineral, their relative crystallographic orientation (RCO) has a negligible effect on the calculation of the entrapment conditions (see Mazzucchelli et al., 2019).

However, when we move to completely anisotropic host-inclusion systems (e.g. quartz in zircon) the situation is more complex (see case iv above and Fig. 1e). Even if the quartz crystal is entrapped in a zircon host at external hydrostatic conditions, when the external P and/or T are changed away from entrapment the strain field applied to the inclusion can become non-uniaxial and will depend on the relative orientation of the host and the inclusion. Therefore, the *a* and *b* axis of the quartz inclusion may be deformed by different amounts, and the angles α, β, γ can change from those required by trigonal symmetry. Therefore we expect that the quartz inclusions in natural zircon crystals are, in general, not trigonal (Gonzalez et al., 2021). These deformations of the quartz unit cell that break the symmetry of the crystal can be described as 'symmetry-breaking strains' (Carpenter et al., 1998; Salje et al., 1993). The effects of symmetry-breaking strains have been observed in cubic garnet hosts adjacent to inclusions as birefringence haloes (e.g. Campomenosi et al., 2020; Howell et al., 2010), however the effects of symmetry breaking on the strain state of the inclusion phase are poorly understood. In particular, when the quartz crystal is no longer trigonal, the key question is whether using the phonon-mode Grüneisen tensor of trigonal α-quartz (for example) to calculate the inclusion strains results in significant errors in the strains and mean stresses, and whether these errors lead to geologically significant errors in the calculation of inclusion entrapment conditions during metamorphism.

To answer this question, we calculated the expected deformation of quartz inclusions entrapped in a zircon host in multiple RCOs and at various hydrostatic geologically relevant P-T conditions. We then performed ab initio Hartree-Fock/Density Functional Theory (HF/DFT) simulations on the deformed α-quartz to determine the Raman shifts for quartz inclusions entrapped at these conditions. This enabled us to determine (i) the error introduced by using the phonon-mode Grüneisen tensor of trigonal quartz, (ii) the inclusion stress states and (iii) the entrapment conditions of inclusions whose symmetry has been broken. Despite we specifically address the case of external hydrostatic conditions, our general conclusions regarding the Raman response to symmetry breaking strains are not just limited to this case. Since the Raman response to the strain state of the inclusion does not depend on the specific conditions that have generated that strain, our analysis of Raman shifts still apply when the external stress is non-hydrostatic, or when the symmetry breaking strains are induced by the geometrical features of the system (morphology of the inclusion, its proximity to other inclusions or to free surfaces). These results can also be applied to quartz inclusions with non-homogeneous strain states, provided that the gradients are small at the spatial resolution of the Raman analysis.

2. Methods

The strains developed in an inclusion depend on the elastic properties of the host and inclusion minerals and the P-T conditions at entrapment. Strains of measured quartz inclusions are defined in terms of the fractional change in the unit-cell parameters of the quartz inclusion relative to a free crystal at ambient conditions (Nye, 1957) . We use the Lagrangian infinitesimal definition of strains, with the convention that the Cartesian axes are aligned with the *Z*-axis parallel to the crystallographic *c*-axis, and the X-axis parallel to the crystallographic *a*-axis. Thus, for example, the strain $\varepsilon_{33} = \frac{c}{c_0} - 1$ is simply the fractional difference in the *c*-lattice parameter of the strained inclusion from the lattice parameter c_0 of a free quartz crystal at ambient conditions. If the quartz remains trigonal then the *a* and *b* unit-cell parameters remain equal, so $\varepsilon_{11} = \varepsilon_{22}$ and the unit-cell angles remain fixed so that the three shear-strain components ε_{23}, ε_{13}, and ε_{12} remain zero. Symmetry breaking is represented by the violation of one or more of these constraints on the strain components.

The calculation of the final inclusion strains for each of our three entrapment conditions proceeded in several steps (Gonzalez et al., 2021). First the changes in the unit-cell parameters of the zircon host crystal from entrapment conditions to ambient conditions were calculated from the axial and volume EoS of zircon (Ehlers et al., 2022). From these changes the deformation tensor of the zircon was calculated, transformed according to the chosen RCO and applied to the quartz inclusion. In combination with the axial and volume EoS of quartz (Alvaro et al., 2020; Angel et al., 2017a), this gives the cell parameters and strains of the inclusion that result from confinement by the zircon host without considering the mutual elastic interaction of the two minerals (Angel et al., 2014b; Gonzalez et al., 2021). The second step of the calculation is required to bring the system to mechanical equilibrium. The elastic relaxation is calculated as the change in strain (and stress) that leads to stress balance in the system assuming elastic behavior, and therefore it reduces the strains in the inclusion to those measured in the laboratory (Angel et al., 2014b) Therefore, the final strains of the inclusion are obtained after accounting for the mutual elastic relaxation of the host and inclusion, and they are calculated using the relaxation tensor which depends on the elastic properties of both minerals, their mutual orientation and the shape of the inclusion (Mazzucchelli et al., 2018; Mazzucchelli et al., 2019) We used the relaxation tensors calculated numerically using finite elements by (Gonzalez et al., 2021) for our chosen RCOs to obtain the final relaxed strains and cell parameters of quartz inclusions apparently entrapped at eclogite and granulite conditions (Table 1a and 1b).

We performed analyses for quartz inclusions entrapped in a non-metamict zircon host for two representative metamorphic entrapment conditions, one in the eclogite metamorphic facies and one in the granulite facies, and a third case of entrapment at the limit of the stability field of quartz near the quartz-coesite phase boundary. Because the two minerals have anisotropic elastic properties, the strains developed in a

Table 1a
Symmetry-breaking strain tensor components (In *Voigt* notation) of the inclusions.

	quartz_eclogite	quartz_granulite	quartz_coesite
ε_1	−0.00636	0.00687	−0.00837
ε_2	−0.00788	0.00750	−0.01124
ε_3	−0.00601	0.00337	−0.00967
ε_4	0.00252	0.00048	0.0048
ε_5	0.00000	−0.00076	0.00000
ε_6	0.00000	0.00106	0.00000

Cartesian axes for the tensors are aligned with the Z-axis parallel to the crystallographic *c*-axis, and the X-axis parallel to the crystallographic *a*-axis. Final relaxed strains for eclogite and granulite. Final unrelaxed strains for the coesite case.

Table 1b
Unit-cell parameters used in the HF/DFT simulations.

	quartz_ref	*quartz_eclogite*	*quartz_granulite*	*quartz_coesite*
a (Å)	4.92825	4.89696	4.96211	4.88699
b (Å)	4.92825	4.8912	4.96207	4.87629
c (Å)	5.42395	5.39136	5.44223	5.37152
V (Å^3)	114.086	111.789	116.1178	110.773
α (°)	90	89.874	89.955	89.761
β (°)	90	90	90.043	90
γ (°)	120	120.039	119.94	120.073

The resulting crystallographic structures for all the three cases have a triclinic symmetry as indicated by $a \neq b$ and the deviation of the unit-cell angles from 90° and 120°.

quartz inclusion within zircon and thus, the amount of symmetry breaking in the quartz, also depend on the RCO of the two crystals (Gonzalez et al., 2021). If the RCO is such that the *c*-axes of zircon and quartz are aligned to one another, there are no symmetry-breaking strains in the quartz inclusion. We therefore selected RCOs from the calculations of (Gonzalez et al., 2021) that gave the greatest amount of symmetry breaking (see Table S1) reducing the symmetry of quartz from non-centrosymmetric trigonal to non-centrosymmetric triclinic ($P3_121$ or $P3_221$ to $P1$). The first case corresponds to a quartz inclusion entrapped in the zircon host at eclogite facies conditions at 2.2 GPa and 650 °C in the "stiff-RCO" with the quartz inclusion rotated −50.27° around the X-axis because this orientation produced the largest magnitude symmetry-breaking strains. The second case corresponds to a quartz inclusion entrapped at the granulite facies at 0.6 GPa and 725 °C in the "soft-RCO" with a quartz inclusion rotated −54.09° around the X-axis, −54.40° around the Y-axis, and 29.40° around the *Z*-axis (see Gonzalez et al. (2021) for the conventions followed for rotations). In this orientation the magnitude of the symmetry-breaking strains is less, but the strains are more affected by mutual elastic relaxation (Gonzalez et al., 2021; Mazzucchelli et al., 2019). We also investigated the effect of symmetry breaking on a quartz inclusion in the stiff-RCO entrapped in a zircon host at 3 GPa and 927 °C near to the quartz-coesite phase boundary (Bose and Ganguly, 1995). This P-T condition provides a practical upper limit to quartz inclusion apparent entrapment and therefore represents the near-maximum effect of the entrapment P-T conditions on the symmetry breaking of the quartz inclusion.

The relaxed inclusion pressures are 0.76 GPa and − 0.65 GPa for the eclogite and granulite examples. For the coesite-boundary simulation, the relaxation was not calculated because we were interested in finding the greatest magnitude of symmetry-breaking strains and, for these entrapment conditions, the mutual elastic relaxation reduces the symmetry-breaking strains. The unrelaxed inclusion pressure for this case is calculated to be ca. 1.1 GPa.

Raman spectra of these triclinic quartz inclusions were then calculated with the same ab initio simulation methods described in (Murri et al., 2018; Murri et al., 2019). In brief, the unit-cell parameters were fixed to the corresponding triclinic parameters calculated for the inclusions from the three different entrapment conditions (Table 1b), and the atomic positions were optimized to minimize the total energy of the crystal. From the resulting atomic configuration, the frequencies of the phonons (normal mode vibrations) can be calculated, including the modes that give rise to peaks in measured Raman spectra. Ab initio hybrid HF/DFT simulations were performed with the CRYSTAL17 code (Dovesi et al., 2018) by employing the same WC1LYP functional as in (Murri et al., 2018; Murri et al., 2019). For the numerical integration of the DFT functionals, the XXLGRID grid was chosen; the effectiveness of such a grid is very high, as it can be estimated by the integration of the electron density of the unit cell, which provides 90.000005 electrons out of 90 for the reference volume at the *static limit* (no zero-point and thermal pressures due to vibrational effects; (Prencipe et al., 2011) and at a pressure of 0 GPa. The localized contracted atomic basis sets used were the same as those employed by (Murri et al., 2018; Murri et al., 2019) [i.e. Si 86-311G** (Pascale et al., 2005) and 8-411G(2d) (Valenzano et al., 2006) for Si and O, respectively].

The unit-cell parameters were fixed at the chosen strain conditions and only the fractional coordinates were optimized at the WC1LYP level (at the static limit) by means of the keyword ATOMONLY (Civalleri et al., 2001; Dovesi et al., 2014) of the CRYSTAL17 code. Vibrational wavenumbers of all of the normal modes were calculated at the Γ point within the limit of the harmonic approximation (see Murri et al., 2019 for further details). The reference simulation of an unstrained trigonal quartz was performed with the same basis set and identical settings to provide the Raman spectrum to be used as the unstrained reference. Structural and vibrational data are reported in the deposited crystallographic information files (cifs) that contain the results of all the simulations that we performed.

3. Results

3.1. Structure

The strains imposed on the quartz inclusions by their host zircon crystals reduce the symmetry of the quartz to triclinic (see Table 1b). This symmetry breaking means that the positions of the 3 Si atoms and the 6 O atoms within the unit-cell of quartz are no longer related by symmetry and are independent of one another. As a consequence, there are three symmetrically independent SiO_4 tetrahedra within the primitive unit-cell, which can have bond lengths, bond angles, and mutual orientations that differ from one another. It is these differences that give rise to additional Raman peaks arising from a splitting or change in the activity of parent trigonal phonon modes. Indeed, the HF/DFT simulations show that structurally-equivalent O-Si-O bond angles within the SiO_4 tetrahedra differ by up to 0.5° between the tetrahedra in each structure. The range of Si-O-Si bond angles between the tetrahedra is 0.2–0.3° and the differences between equivalent Si—O bond lengths in the tetrahedra in each structure range up to 0.005 Å. The internal O-Si-O angles of the tetrahedra also differ by up to 0.5° from the values found in the hydrostatic simulations at the same pressure (Murri et al., 2019) and the Si-O-Si angles are increased by 0.2°-0.3°. Despite these internal differences in bond angles, the volumes of the SiO_4 tetrahedra are the same as those of trigonal quartz. This shows that symmetry breaking is mostly accommodated structurally by small shears and tilts of the SiO_4 tetrahedra. These structural changes are similar to those that occur in the trigonal structure of quartz under shear strains that do not break the symmetry (Murri et al., 2019), but with the difference that the shears and tilts are not the same for every tetrahedron within the symmetry-broken structures.

3.2. Raman modes

Results of the HF/DFT simulations show that symmetry breaking induces small changes in the structure of quartz which also correspond to small changes in the observed Raman spectra. This allows us to compare directly the corresponding 'parent' modes of the trigonal quartz structure with those calculated from the symmetry-broken quartz structures. This reveals several slight differences between the corresponding Raman spectra. First, the reduction in symmetry of the structure means that the symmetries of the modes themselves change. Trigonal quartz has A_1, A_2 and E modes, of which only the A_1 and E modes are Raman active, while A_2 are infrared active. In triclinic symmetry all of the modes become A modes and all are both Raman and infrared active (Aroyo et al., 2011). However, the HF/DFT simulations show that for this degree of symmetry breaking and structural distortion, the Raman inactive A_2 modes of the trigonal structure do not develop any significant Raman activity in the triclinic structure and their calculated intensities all remain less than 10^{-5} of the most intense Raman mode. Therefore, the symmetry breaking does not result in any additional detectable Raman peaks stemming from the apparent A_2 modes under conventional experimental conditions (Fig. 2).

The Raman-active A_1 modes in trigonal quartz are non-polar, but when the symmetry is reduced to triclinic they transform into polar modes of A symmetry. Polar optical modes show the so-called LO-TO splitting, that is, they have longitudinal optical (LO) and transverse optical (TO) components that appear at different wavenumbers with a difference $\Delta\omega_{LO\text{-}TO} = \omega_{LO} - \omega_{TO}$. For such modes, not only the intensities but also the positions of the corresponding Raman peaks depend on the scattering geometry, namely the orientation of the net crystal polarization with respect to the polarization of the incident light. In a random orientation, the two components will mix into quasi phonons and may

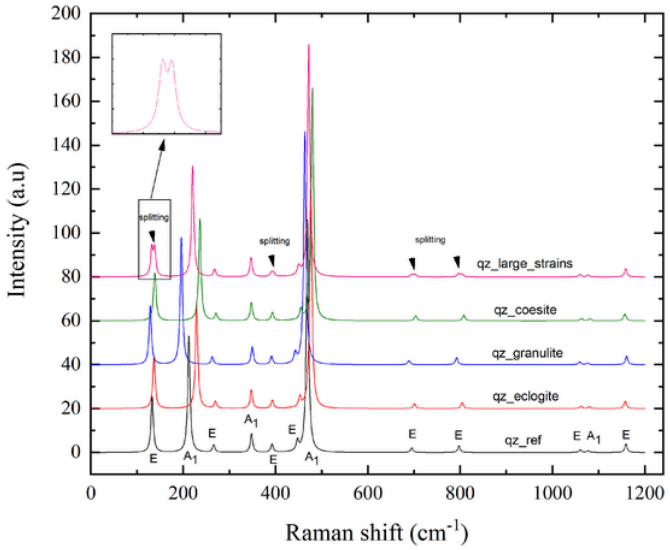

Fig. 2. Comparison of the calculated Raman spectra of inclusions labelled by entrapment conditions with the reference spectra of an unstrained quartz crystal (bottom) and an extreme non-realistic case of large symmetry-breaking strains (top). The symmetry labels for the modes (E and A_1) refer to trigonal reference quartz. All Raman spectra were simulated with a FWHM (Full Width at Half Maximum) of 5 cm^{-1} and with a Lorentzian line shape. This FWHM is that measured for the band near to 128 cm^{-1} in natural quartz at ambient conditions by using a Raman spectrometer with a resolution of 2 cm^{-1} (Morana et al., 2020).

produce two Raman peaks with a wavenumber difference $\Delta\omega_{LO\text{-}TO}$ depending on the angle of inclination between the net polarization and the incident-light polarization. However, for the triclinic A modes coming from trigonal A_1 modes the maximum $\Delta\omega_{LO\text{-}TO}$ is less than 0.06 cm^{-1} and therefore it will not result in any detectable change of Raman signal as a function of the crystal orientation. In trigonal quartz the E modes already exhibit LO-TO splitting, whose magnitude depends on the phonon polarity and can be of up to 174 cm^{-1} (for the mode near 1060 cm^{-1}, see Table S2). The symmetry breaking from trigonal to triclinic means that effectively each E mode evolves into two A modes in triclinic and both of these A modes themselves exhibit LO-TO splitting; thus each E mode of the trigonal Raman spectra will now appear as a doublet, whose components may shift with the orientation of the crystal due to their LO-TO splitting. However, for the natural inclusion cases (i.e. eclogite and granulite cases) the split between all pairs of A modes coming from each E parent mode is less than 0.88 cm^{-1}, while for the coesite boundary case the maximum splitting is 1.82 cm^{-1} for the first pair of A modes (see Table 2). Such peak splitting is in general detectable with high-resolution Raman spectrometers, but most of the commercially-available spectrometers have an instrumental resolution of ~2 cm^{-1}. In this case the peak splitting would likely not be resolvable but may produce detectable peak broadening if the split phonon modes have similar intensities. Similarly, peak-shape asymmetry could be observed if one of the split phonon modes is more intense than the other. Splitting of the order of 5–6 cm^{-1} can be achieved only when the symmetry-breaking component of the strains approaches 0.01 in magnitude, as shown in the example in Fig. 2, labelled 'large strains'. The LO-TO splitting of individual triclinic A modes arising from trigonal E modes is about the same in magnitude as their parent modes in trigonal (see Table S2) even for the coesite case. Thus, examination of the LO-TO splitting does not indicate whether or not symmetry-breaking strains are present in the inclusion. Moreover, the detection of the LO-TO splitting requires the appropriate orientation of the crystal with respect to the scattering geometry (Shapiro and Axe, 1972). In particular, the crystal must be oriented in different directions in order to see both of the components. This procedure is easily performed with free crystals, but when dealing with host inclusion systems it becomes challenging because of the limited accessible orientations of the inclusion imposed by it being buried in its' host, together with possible symmetry and polarization mixing (e.g. Shapiro and Axe, 1972), and peak overlaps due to the presence of the host mineral (Fig. S1).

Table 2
Wavenumbers (cm^{-1}) of Raman and IR active-modes from the HF/DFT simulations at the *static limit*.

Mode symm_ trigonal	*quartz_ ref*	*Mode symm_ triclinic*	*quartz_ eclogite*	*quartz_ granulite*	*quartz_ coesite*
	TO (cm^{-1})		*TO (cm^{-1})*		
E(R, IR)	133.13	A(R, IR)	136.77	128.99	137.92
		A(R, IR)	137.59	129.13	139.74
A_1(R)	212.72	A(R, IR)	229.50	196.32	236.47
E(R, IR)	266.43	A(R, IR)	269.82	263.31	271.36
		A(R, IR)	270.21	263.53	271.91
A_1(R)	348.42	A(R, IR)	348.03	349.82	348.10
A_2 (IR)	353.81	A(R, IR)	351.37	357.03	350.29
E(R, IR)	392.73	A(R, IR)	393.33	391.42	393.50
		A(R, IR)	393.37	392.08	393.62
E(R, IR)	447.81	A(R, IR)	452.86	442.65	454.91
		A(R, IR)	453.31	443.37	455.67
A_1(R)	469.62	A(R, IR)	476.77	463.92	480.39
A_2 (IR)	503.39	A(R, IR)	511.28	495.18	514.61
E(R, IR)	695.30	A(R, IR)	701.16	689.10	703.54
		A(R, IR)	701.76	689.64	704.66
A_2 (IR)	774.55	A(R, IR)	776.85	772.72	778.37
E(R, IR)	797.68	A(R, IR)	804.63	792.08	808.04
		A(R, IR)	804.89	792.67	808.35
E(R, IR)	1060.35	A(R, IR)	1061.96	1059.03	1062.79
		A(R, IR)	1062.41	1059.28	1063.56
A_2 (IR)	1068.49	A(R, IR)	1071.75	1065.05	1072.96
A_1(R)	1077.31	A(R, IR)	1079.93	1075.99	1081.30
E(R, IR)	1159.50	A(R, IR)	1157.38	1160.68	1156.25
		A(R, IR)	1158.26	1161.10	1157.83

R: Raman-active, IR: infrared-active; phonons that are IR active carry polarity and therefore exhibit LO and TO components.

In principle the intensities of the modes, both in parallel polarized 'HH' and cross polarized 'VH' spectra (see Campomenosi et al., 2020), can be analysed in order to detect symmetry-breaking strains. However, under realistic conditions, the ab initio simulations do not show any particular trend that could be indicative of symmetry-breaking strains. In detail, the two A modes derived from the trigonal E modes have a similar pattern of intensities to their parent modes in trigonal quartz with the A intensities being half of the E modes for both HH and VH configurations. A modes from A_1 have similar intensity components (in terms of absolute values), while as mentioned above, A modes coming from A_2 are Raman active but with intensities close to zero (see deposited cif file). Therefore, when the splitting of the two A modes coming from an E mode is not sufficient to individually resolve them, the intensity contributions of the A modes will sum up giving rise to a single peak as shown in Fig. 2 for the eclogite, granulite and coesite cases.

As a consequence, for geologically relevant inclusion entrapment conditions, the Raman spectrum of a quartz inclusion in zircon host is expected to show similar features to that of a free quartz crystal. The major exception is that the Raman peak positions from the quartz inclusions will differ based on the entrapment conditions (i.e. the magnitude of the inclusion pressure) and the applied strain from the zircon host. If the quartz inclusion is, however, subjected to large degrees of symmetry breaking, we then may observe broadening or asymmetry of Raman peaks, or even splitting of the trigonal E modes if the instrumental resolution of the available spectrometer is sufficient. The question then is whether these differences between the Raman spectra of triclinic quartz inclusions and trigonal quartz are large enough to induce significant er-

rors into the calculations of inclusion stress states and thus inferred entrapment conditions.

4. Implications for Raman piezo-barometry

4.1. Inclusion remnant pressures and hydrostatic pressure calibrations

Hydrostatic pressure calibrations of Raman wavenumber shifts as a function of pressure (e.g. Morana et al., 2020; Schmidt and Ziemann, 2000) are frequently used to estimate the remnant pressures of quartz inclusions for the application of elastic geothermobarometry. The problems with this approach, generally in the context of a quartz inclusion in a garnet host, have previously been explained in detail (e.g. Angel et al., 2019; Gilio et al., 2021; Gonzalez et al., 2019; Murri et al., 2018), but have not been evaluated for quartz inclusions contained in elastically anisotropic host minerals such as zircon.

Here we can test the use of hydrostatic pressure calibrations by using them to infer from the Raman shifts calculated in our DFT simulations the residual pressures in the inclusions. For these tests we used the quartz hydrostatic calibration equations of Schmidt and Ziemann (2000) for the 206 and 464 cm^{-1} bands, Thomas and Spear (2018) for the 128 cm^{-1} band, and Morana et al. (2020) for the 128, 206, 265, 464, 696, 809, 1080, and 1161 cm^{-1} bands (Table S3). In general, the resulting "pressures" indicated by each individual mode are significantly different from one another (Fig. 3, Table S3) and there is a large variation in the discrepancy between the hydrostatic calibration results and the true mean stress of the symmetry-broken inclusion. The biggest discrepancy is for the 1080 cm^{-1} which can yield inclusion pressures more than 1 GPa different from the true pressure (Fig. 3). Therefore, the apparent entrapment conditions obtained by measuring single modes and using the hydrostatic calibrations are dependent on the Raman band selected for interpretation. Though the data in Fig. 3 appear

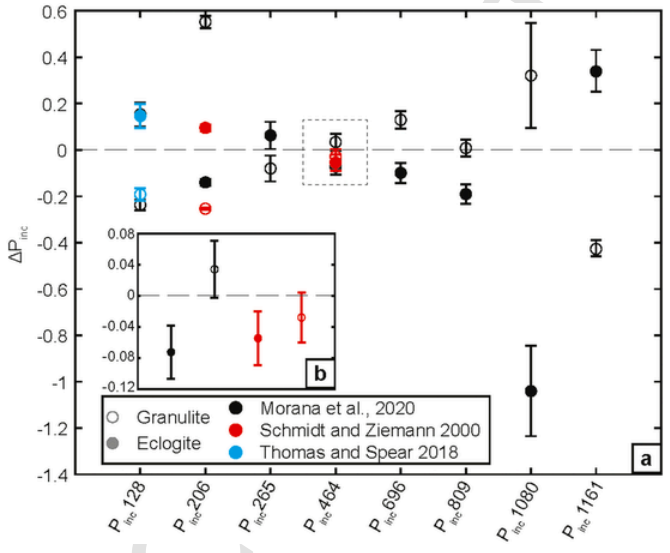

Fig. 3. Inclusion pressures in symmetry-broken inclusions determined from the hydrostatic calibrations of the shifts of individual Raman lines plotted as the difference from the true mean stress in the inclusion (ΔP_{inc}). a) Plot of the P_{inc} discrepancies from all of the calibrated Raman modes available. The dashed outline box indicates the area plotted in (b). b) P_{inc} discrepancy for the frequently used 464 cm^{-1} band of quartz. Error bars were determined assuming a 0.3 cm^{-1} uncertainty on the Raman band position which is consistent with typical laboratory Raman spectrometers (Bonazzi et al., 2019; Gonzalez et al., 2019). Open symbols are the granulite case, closed symbols the eclogite case. Hydrostatic calibrations of individual lines are indicated by symbol color, black for Morana et al. (2020), red for Schmidt and Ziemann (2000), and blue for Thomas and Spear (2018). (For interpretation of the references to color in this figure legend, the reader is referred to the web version of this article.)

to suggest that the 464 cm^{-1} band would provide a reasonable Pinc estimate, we emphasize that this approach is still inherently incorrect because it is not consistent with the other Raman band "pressures" or within the uncertainties of the dPinc = 0 line. Furthermore, unlike the quartz-in-garnet system which is not affected by the RCO, the deviatoric stresses on a quartz inclusion in a zircon are dependent on the orientation, implying that the discrepancy between the hydrostatic calibrations and true inclusion pressure cannot be predicted in a straightforward manner. Based on the facts that individual Raman bands yield different "pressures" and that the discrepancies as a function of orientation cannot be simply predicted, we conclude that the hydrostatic calibrations of wavenumber shifts with pressure should not be applied to the quartz-in-zircon elastic system to estimate the residual inclusion pressure. As shown in Table S3, this practice will yield over- or underestimated inclusion pressures and entrapment conditions, and lead to incorrect geological interpretations.

4.2. Residual inclusion strains, stress, and pressure: The phonon-mode Grüneisen tensor approach

The strains of quartz inclusions are calculated from the measured Raman wavenumber shifts using the trigonal phonon-mode Grüneisen tensor (Angel et al., 2019; Barron et al., 1982; Cantrell, 1980; Murri et al., 2018; Murri et al., 2019; Ziman, 1960):

$$\frac{-\Delta\omega^m}{\omega_0^m} = 2\gamma_1^m\varepsilon_1 + \gamma_3^m\varepsilon_3 \quad (1)$$

in which $\Delta\omega^m$ is the difference between the wavenumber of the Raman mode in the inclusion from $\omega_0{}^m$ the wavenumber of the same mode of a free quartz crystal at ambient conditions. The $\gamma_1{}^m$and $\gamma_3{}^m$ are components of the Grüneisen tensor (in Voigt notation, see S·I and Angel et al. (2019) for further details) of phonon mode *m*. This approach implicitly assumes that the tensor components $\gamma_1{}^m$and $\gamma_2{}^m$ are equal and that the tensor components $\gamma_4{}^m = \gamma_5{}^m = \gamma_6{}^m = 0$ because of the trigonal symmetry of quartz (Nye, 1985). When the symmetry of quartz is broken, these restrictions on the tensor components are removed, Eq. 1 is no longer valid and we have to consider the general formulation for the triclinic case (Angel et al., 2019):

$$\frac{-\Delta\omega^m}{\omega_0^m} = \gamma_1^m\varepsilon_1 + \gamma_2^m\varepsilon_2 + \gamma_3^m\varepsilon_3 + \gamma_4^m\varepsilon_4 + \gamma_5^m\varepsilon_5 + \gamma_6^m\varepsilon_6 \quad (2)$$

However, the values of these tensor components for quartz with triclinic symmetry are not available and their calculation would require extensive HF/DFT simulations. Furthermore, as we have shown, when an inclusion is measured by Raman spectroscopy it is difficult to determine from inspection of the spectra (Fig. 2) whether or not its symmetry remained trigonal or has been broken by elastic interaction with the host. Therefore, it is useful to evaluate the error introduced into estimated entrapment conditions by ignoring the effects of symmetry breaking. For these tests we used the Raman peak positions calculated from HF/DFT simulations in conjunction with the trigonal Grüneisen tensor of quartz at 0 K to recalculate the inclusion strains, stresses, and entrapment conditions (values of the Grüneisen tensor components are reported in Table S4). The values obtained can be then compared against the real values which account for the effects of symmetry breaking (Table 1a).

For all three cases the strains were calculated from the Raman wavenumber shifts of three sets of Raman modes: i) all modes, ii) 133, 212, 469 cm^{-1} (HF/DFT values which correspond to the following experimental values: 128, 206 and 464 cm^{-1}) and iii): 133, 469, 695 cm^{-1} (which correspond to the experimental values: 128, 464, 697 cm^{-1}). For each set of Raman modes, the strains were calculated by means of the trigonal phonon-mode Grüneisen tensor of quartz using the stRAinMAN software (Angel et al., 2019). Then, the strains were used with the

rescaled (Mazzucchelli et al., 2021) elastic moduli at 1 bar of Lakshtanov et al. (2007) to determine the inclusion mean stress (i.e. Pinc) at room temperature (25 °C; Bonazzi et al., 2019). The strains obtained using the trigonal phonon-mode Grüneisen tensor and the corresponding inclusion mean stresses are reported in Table 3.

Application of the trigonal phonon-mode Grüneisen tensor assumes that the inclusion symmetry is not broken and therefore the constraints of the trigonal symmetry are valid. Therefore, only the strains that conform to trigonal symmetry are obtained, with $\varepsilon_1 = \varepsilon_2 \neq \varepsilon_3$. These values are different from the real strains (Table 1b) where $\varepsilon_1 \neq \varepsilon_2$ and the components $\varepsilon_4, \varepsilon_5, \varepsilon_6$ are non-zero. This assumption affects the determined inclusion stresses and average pressures (P_{thermo} for the unrelaxed strains, P_{inc} for the relaxed strains) causing slight differences between the symmetry broken and trigonal Grüneisen cases (see Table 3). Furthermore, the strains determined from these calculations vary slightly depending on the subset of Raman modes that is used, because the different Raman modes have different sensitivities to each strain component as they have different values for the components of their phonon-mode Grüneisen tensors. This can also be seen in the slopes of the isoshift lines when plotted against the strains (see Murri et al., 2018).

As a consequence of these variations in sensitivity the resulting inclusion pressures (i.e. P_{inc} and P_{thermo}) for the three different sets of Raman modes (i.e. all modes; 128, 206, 464 cm^{-1} and 128, 464, 695 cm^{-1}) using the trigonal phonon-mode Grüneisen approach differ slightly (Table 3) but are always less than the real pressure values by <0.1 GPa. However, in practice it is not feasible to use all of the quartz Raman bands to calculate the inclusion strain because there are peak overlaps from the host mineral (see Fig. S1). The problem is even worse when the host mineral has a high absorbance, such as zircon, which produces an intense Raman signal that masks the signal from the underlying quartz inclusion. In previous studies of quartz inclusions (typically contained in garnet), the 128, 206, and 464 cm^{-1} bands are generally used for the determination of residual strain (e.g. Bonazzi et al., 2019). When using this phonon-mode combination, we obtain inclusion pressure values of 0.736 GPa, −0.751 GPa, and 1.025 GPa, compared to the real P_{inc} and P_{thermo} (quartz-coesite case) calculated from the symmetry-breaking strains of 0.757, −0.648 and 1.102 GPa for the eclogite, granulite and quartz-coesite cases, respectively. But on the basis of experimental experience with quartz in zircon host-inclusion systems, this band combination is often not usable because of the interfering peak overlaps on the 206 cm^{-1} band (see Fig. S1). Therefore, a more realistic phonon-mode combination for the determination of inclusion strains is the 128, 464, and 695 cm^{-1} bands, where there is generally less interference from the zircon host, so hereafter only this case from the trigonal approach will be discussed. When this phonon-mode combination is used for the calculation of the inclusion pressures, we obtain values of 0.727 GPa, −0.659 GPa, and 1.057 GPa, which yields errors of 0.03, 0.01, and 0.05 GPa with respect to the real inclusion pressures (Table 3). These results suggest that application of the trigonal quartz phonon-mode Grüneisen tensor to calculate the residual pressure from a Raman measurement of a slightly symmetry-broken inclusion will result in generally small errors that would typically fall within the uncertainty of the Raman measurements. However, in order to determine whether these

Table 3
Strains, Pinc and Ptrap determinations.

	Trigonal approach_1 (All_modes)			*Trigonal approach_2 (128,206,464)*			*Trigonal approach_3 (128,464,695)*		
	ECL	GRAN	COE	ECL	GRAN	COE	ECL	GRAN	COE
	P = 2.2GPa / T = 650 °C	*P = 0.6 GPa/ T = 725 °C*	*P = 3 GPa/ T = 927 °C*	*P = 2.2GPa / T = 650 °C*	*P = 0.6 GPa/ T = 725 °C*	*P = 3 GPa/ T = 927 °C*	*P = 2.2GPa / T = 650 °C*	*P = 0.6 GPa/ T = 725 °C*	*P = 3 GPa/ T = 927 °C*
ε_1	−0.00677	0.00820	−0.00917	−0.00697	0.01011	−0.00814	−0.00660	0.00698	−0.00914
ε_2	−0.00677	0.00820	−0.00917	−0.00697	0.01011	−0.00814	−0.00660	0.00698	−0.00914
ε_3	−0.00608	0.00309	−0.00943	−0.00578	0.00101	−0.01060	−0.00616	0.00395	−0.00972
P_{inc}	0.736	−0.707	–	0.736	−0.751	–	0.727	−0.659	–
P_{thermo}	0.973	−0.876	1.048	0.973	−0.920	1.025	0.960	−0.819	1.057
P_{trap_iso} trig	2.135	0.575	2.803	2.135	0.572	2.774	2.118	0.585	2.815
P_{trap_aniso} trig	2.192	0.592	2.951	2.196	0.503	2.906	2.176	0.602	2.966
	Symm break Approach			*Symm break Approach*			*Symm break Approach*		
ε_1	−0.00636	0.00687	−0.00837	−0.00636	0.00687	−0.00837	−0.00636	0.00687	−0.00837
ε_2	−0.00788	0.00750	−0.01124	−0.00788	0.00750	−0.01124	−0.00788	0.00750	−0.01124
ε_3	−0.00601	0.00337	−0.00967	−0.00601	0.00337	−0.00967	−0.00601	0.00337	−0.00967
ε_4	0.00252	0.00048	0.0048	0.00252	0.00048	0.0048	0.00252	0.00048	0.0048
ε_5	0.00000	−0.00076	0	0.00000	−0.00076	0	0.00000	−0.00076	0
ε_6	0.00000	0.00106	0	0.00000	0.00106	0	0.00000	0.00106	0
P_{inc}	0.757	−0.648	–	0.757	−0.648	–	0.757	−0.648	–
P_{thermo}	1.001	−0.806	1.102	1.001	−0.806	1.102	1.001	−0.806	1.102
P_{trap_iso} sb	2.171	0.588	2.873	2.171	0.588	2.873	2.171	0.588	2.873
P_{trap_aniso} sb	2.200	0.600	3.000	2.200	0.600	3.000	2.200	0.600	3.000
P_{inc}_sb- P_{inc} trig	0.021	0.059		0.020	0.103		0.030	0.011	
P_{thermo} sb- P_{thermo} trig	0.028	0.070	0.055	0.028	0.114	0.077	0.041	0.013	0.045
P_{trap_iso} sb - P_{trap_iso} trig	0.036	0.013	0.070	0.036	0.016	0.099	0.053	0.003	0.058
P_{trap_aniso} sb- P_{trap_iso} trig	0.065	0.025	0.197	0.065	0.028	0.226	0.082	0.015	0.185
P_{trap_aniso} sb - P_{trap_aniso} trig	0.008	0.008	0.049	0.004	0.097	0.094	0.024	−0.002	0.034

N·B: All pressure values are in GPa.

errors in the inclusion pressures lead to geologically significant errors in the calculation of inclusion entrapment conditions, the entrapment pressures have been calculated and discussed in the framework of both isotropic and anisotropic models.

4.3. Recalculation of apparent entrapment pressures: isotropic model

The same volume EoS for quartz (Angel et al., 2017a) and zircon (Ehlers et al., 2022) used for the original calculation of inclusion strains have been used for the calculation of isotropic entrapment isomekes by means of the EosFit7-Pinc software (Angel et al., 2017b). The entrapment isomeke is a path in P-T space where the fractional volume changes of both the host and the inclusion phases remain equal to one another but non-zero (e.g. Adams et al., 1975; Rosenfeld and Chase, 1961).When the P_{inc} from the fully symmetry-broken strains is used in the isotropic model, the entrapment pressures are 2.171 GPa for the eclogite facies, 0.588 GPa for the granulite facies, and 2.873 GPa for the coesite-quartz case. The discrepancies, with respect to the preset entrapment conditions (see Table 3), occur because of the assumed isotropic behavior during the back calculation of the entrapment conditions and are in agreement with similar tests performed by (Gonzalez et al., 2021). If instead we take the P_{inc} that is calculated from the strains using the trigonal quartz Grüneisen tensor, we obtain P_{trap} estimates that even further underestimate the original entrapment conditions. For the P_{inc} values calculated using the 128,464 and 695 cm^{-1} modes, we obtain P_{trap} values of 2.118 GPa for the eclogite facies, 0.585 GPa for the granulite facies, and 2.815 GPa for the coesite-quartz boundary and this gives discrepancies of 0.082 GPa, 0.015 GPa, and 0.185 GPa with respect to the preset entrapment conditions. These discrepancies represent the errors introduced by assuming that (i) the inclusion is trigonal with no symmetry-breaking when the strain is obtained from Raman measurements, and (ii) the host and inclusion are completely isotropic for the calculation of the entrapment conditions. These results imply that significant errors result from the application of fully isotropic calculations to anisotropic host-inclusion systems (see Table 3). Furthermore, the magnitudes of these errors are dependent on the entrapment conditions and RCO.

4.4. Recalculation of apparent entrapment conditions: anisotropic model

In the anisotropic elastic model, the inverse relaxation tensor was calculated for a given orientation (Table S1) and applied to the trigonal symmetry relaxed strains to determine the unrelaxed strain tensor (Mazzucchelli et al., 2019). The unrelaxed strain tensor was then used in EoSFit7c (Angel et al., 2014a) to calculate the axial isomekes (i.e. curves in P-T space along the crystallographic directions where no strain gradients are developed) of the quartz inclusion using the method of (Alvaro et al., 2020) but extended to lower symmetry host-inclusion systems. This calculation provides the axial isomekes of the quartz inclusion for the directions of quartz parallel to the three crystallographic axes of the zircon host. The entrapment conditions are interpreted as the intersection point of the axial isomekes. As expected, this was verified for each of the three entrapment conditions when the full symmetry broken strain tensor was input to calculate the axial isomekes, meaning that our calculations are internally consistent (see Fig. 4). On the other hand, when the strains from the trigonal quartz Grüneisen tensors are used, the three axial isomekes do not intersect at a single P-T point. This happens because application of the trigonal Grüneisen tensor yields incorrect inclusion strains that conform to the trigonal symmetry but are not to the actual triclinic strains. This result implies that unique entrapment conditions cannot be calculated from symmetry-broken inclusions unless the full symmetry-broken strain tensor is known. Despite this, the results in Fig. 4 show that the average of the three axial isomekes still nearly intersects the original entrapment conditions. Indeed, from the trigonal Grüneisen tensor strains using the 128, 464, and 695 cm^{-1} bands, the calculated entrapment conditions are 2.176 GPa, 0.602 GPa, and 2.966 GPa, giving discrepancies on P_{trap} of 0.024 GPa, −0.002 GPa, and 0.034 GPa (Table 3). These discrepancies demonstrate that the error in the individual axial isomekes and their failure to intersect at one unique PT point results solely from the use of the trigonal quartz phonon mode Grüneisen tensor because all other parts of the calculations are equivalent.

These results suggest that we can still use the trigonal quartz phonon-mode Grüneisen tensor to calculate the entrapment conditions using the anisotropic elastic model. However, in this case an external constraint on either pressure or temperature is still required to deter-

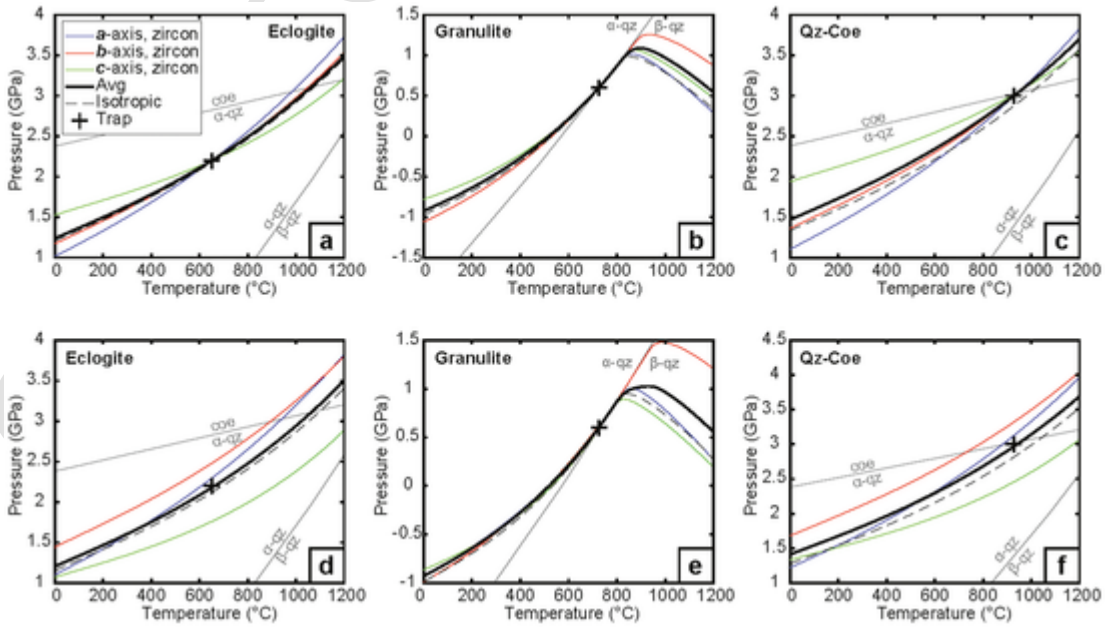

Fig. 4. Axial and volume isomekes calculated for the various sets of entrapment conditions and selected quartz phonon-mode combinations. Figures a-c show the results from the true symmetry-broken strains. Figures d-f show the results from the trigonal strains calculated using the trigonal Grüneisen phonon-mode tensor for the 128, 464 and 695 cm^{-1} modes. The cross in each panel represents the entrapment conditions used for the simulation. Axial isomekes are drawn for the directions of the a,b, and c-axes of the zircon host and their corresponding directions in the quartz inclusion, and their average (black solid line) is labelled 'avg'.

mine the unique entrapment conditions. It is important to note that despite the requirement of an external constraint, this approach yields a smaller error than the use of an isotropic elastic model. Because these errors are relatively small and substantially less than those produced by the errors on measured Raman peak positions, we conclude that the trigonal quartz phonon mode Grüneisen tensor can be used to calculate the strains from slightly symmetry broken quartz inclusions contained in zircon hosts without introducing major uncertainties in the inferred entrapment pressures.

5. Conclusions

We have reported the first study on symmetry breaking strains in quartz by HF/DFT. Ab initio simulations allowed us to avoid the difficulties that would arise if we tried to apply deviatoric stress to quartz experimentally and measure the Raman modes (e.g. Briggs and Ramdas, 1977). These HF/DFT simulations have shown that the changes in the positions of the Raman modes for strains that are expected for real quartz inclusions in zircon are similar to those that would be seen if the quartz inclusions remained truly trigonal in symmetry. But, because the Raman bands of the inclusions do not shift as they would under hydrostatic pressure, the use of the positions of single bands and a hydrostatic calibration leads to incorrect pressure estimates for entrapment of quartz inclusions in zircon.

*V*ery large symmetry-breaking strains can generate a broadening or even a splitting of the Raman modes (see Fig. 2) coming from the parent E modes, and therefore particular attention should be paid to these modes when studying quartz in zircon host-inclusion systems. If no broadening or splitting of the Raman modes is observed, our results show that, even when the inclusion is subjected to symmetry-breaking strains, the measured Raman modes of quartz can be used to calculate the average inclusion pressures with small errors.

These inclusion pressures yield entrapment isomekes with the isotropic model that pass within 0.185 GPa of the true entrapment pressures. The inclusion strains calculated via the trigonal phonon-mode Grüneisen tensors are not correct, as would be expected, so the axial isomekes calculated from them often do not intersect as would be required to define the P and T of entrapment (Alvaro et al., 2020). However, the average of the axial isomeke pressures result in better estimates, within 0.034 GPa of the true entrapment pressures. Therefore, the use of the trigonal phonon-mode Grüneisen tensor to interpret Raman spectra of quartz inclusions in zircon does not introduce geologically significant errors in calculated entrapment pressures within the stability field of α-quartz provided the anisotropic analysis is followed.

Declaration of Competing Interest

The authors declare that they have no known competing financial interests or personal relationships that could have appeared to influence the work reported in this paper.

Acknowledgements

MLM is supported by an A. von Humboldt research fellowship. JPG is supported by a NSF-EAR Postdoctoral Fellowship (No. 1952698). This research has been supported by the ERC-StG TRUE DEPTHS project under the European Union's Horizon 2020 Research and Innovation Programme (n.714936) to M. Alvaro. This work has been partly supported by the PRIN-MUR project "THALES" Prot.2020WPMFE9_003. MA is also supported by the Highlight funded by Fondi regione Lombardia DGR 3776. We thank Marta Morana, Caterina Canovaro and Fabrizio Nestola, Nicola Campomenosi and Yuuki Hagiwara for providing the pictures used in Fig. 1a, b, c and d respectively.

Appendix A. Supplementary data

Supplementary data to this article can be found online at https://doi.org/10.1016/j.lithos.2022.106716.

References

Adams, H.G., Cohen, L.H., Rosenfeld, J.L., 1975. Solid inclusion piezothermometry I: comparison dilatometry. Am. Mineral. 60, 574–583.
Alvaro, M., Mazzucchelli, M.L., Angel, R.J., Murri, M., Campomenosi, N., Scambelluri, M., Nestola, F., Korsakov, A., Tomilenko, A.A., Marone, F., Morana, M., 2020. Fossil subduction recorded by quartz from the coesite stability field. Geology 48, 24–28.
Angel, R.J., Alvaro, M., Miletich, R., Nestola, F., 2017a. A simple and generalised P-T-V EoS for continuous phase transitions, implemented in EosFit and applied to quartz. Contrib. Mineral. Petrol. 172, 29.
Angel, R.J., Gonzalez-Platas, J., Alvaro, M., 2014a. EosFit7c and a Fortran module (library) for equation of state calculations. Zeitschrift fur Kristallographie 229, 405–419.
Angel, R.J., Mazzucchelli, M.L., Alvaro, M., Nestola, F., 2017b. EosFit-Pinc: a simple GUI for host-inclusion elastic thermobarometry. Am. Mineral. 102, 1957–1960.
Angel, R.J., Mazzucchelli, M.L., Alvaro, M., Nimis, P., Nestola, F., 2014b. Geobarometry from host-inclusion systems: the role of elastic relaxation. Am. Mineral. 99, 2146–2149.
Angel, R.J., Murri, M., Mihailova, B., 2019. Stress, Strain and Raman Shifts. Zeitschrift fur Kristallographie 129–140.
Aroyo, M.I., Perez-Mato, J.M., Orobengoa, D., Tasci, E., de la Flor, G., Kirov, A., 2011. Crystallography online: Bilbao Crystallographic Server. Bulg. Chem. Commun. 43, 183–197.
Baldwin, S.L., Schonig, J., Gonzalez, J.P., Davies, H., von Eynatten, H., 2021. Garnet sand reveals rock recycling processes in the youngest exhumed high- and ultrahigh-pressure terrane on Earth. Proc Natl Acad Sci U S A 118.
Barron, T.H.K., Collins, J.F., Smith, T.W., White, G.K., 1982. Thermal expansion, Grüneisen functions and static lattice properties of quartz. J. Phys. C Solid State Phys. 15, 4311–4326.
Bonazzi, M., Tumiati, S., Thomas, J.B., Angel, R.J., Alvaro, M., 2019. Assessment of the reliability of elastic geobarometry with quartz inclusions. Lithos 350–351.
Bose, K., Ganguly, J., 1995. Quartz-Coesite transition Revisited - Reversed Experimental-Determination at 500-1200-Degrees-C and Retrieved Thermochemical Properties. Am. Mineral. 80, 231–238.
Briggs, R.J., Ramdas, A.K., 1977. Piezospectroscopy of the Raman spectrum of α-quartz. Phys. Rev. B 16, 3815–3826.
Campomenosi, N., Mazzucchelli, M.L., Mihailova, B.D., Angel, R.J., Alvaro, M., 2020. Using polarized Raman spectroscopy to study the stress gradient in mineral systems with anomalous birefringence. In: Contributions to Mineralogy and Petrology 175.
Campomenosi, N., Scambelluri, M., Angel, R.J., Hermann, J., Mazzucchelli, M.L., Mihailova, B., Piccoli, F., Alvaro, M., 2021. Using the elastic properties of zircon-garnet host-inclusion pairs for thermobarometry of the ultrahigh-pressure Dora-Maira whiteschists: Problems and perspectives. In: Contributions to Mineralogy and Petrology, 176.
Cantrell, J.H., 1980. Generalized Grüneisen tensor from solid nonlinearity parameters. Phys. Rev. B 21, 4191–4195.
Carpenter, M.A., Salje, E.K.H., Graeme-Barber, A., 1998. Spontaneous strain as a determinant of thermodynamic properties for phase transitions in minerals. Eur. J. Mineral. 10, 621–691.
Cisneros, M., Barnes, J.D., Behr, W.M., Kotowski, A.J., Stockli, D.F., Soukis, K., 2021. Insights from elastic thermobarometry into exhumation of high-pressure metamorphic rocks from Syros, Greece. Solid Earth 12, 1335–1355.
Civalleri, B., D'Arco, P., Orlando, R., Saunders, V., Dovesi, R., 2001. Hartree–Fock geometry optimisation of periodic systems with the CRYSTAL code. Chem. Phys. Lett. 348, 131–138.
Dovesi, R., Erba, A., Orlando, R., Zicovich-Wilson, C.M., Civalleri, B., Maschio, L., Rérat, M., Casassa, S., Baima, J., Salustro, S., Kirtman, B., 2018. Quantum-mechanical condensed matter simulations with CRYSTAL. Wiley Interdiscip. Rev. Comput. Mol. Sci. 8, 1–36.
Dovesi, R., Orlando, R., Erba, A., Zicovich-Wilson, C.M., Civalleri, B., Casassa, S., Maschio, L., Ferrabone, M., De La Pierre, M., D'Arco, P., Noël, Y., Causà, M., Rérat, M., Kirtman, B., 2014. CRYSTAL14: a program for the ab initio investigation of crystalline solids. Int. J. Quantum Chem. 114, 1287–1317.
Ehlers, A.M., Zaffiro, G., Angel, R.J., Boffa-Ballaran, T., Carpenter, M.A., Alvaro, M., Ross, N.L., 2022. Thermoelastic properties of zircon: Implications for geothermobarometry. Am. Mineral. 107, 74–81.
Gilio, M., Angel, R.J., Alvaro, M., 2021. Elastic geobarometry: how to work with residual inclusion strains and pressures. Am. Mineral. 106, 1530–1533.
Gonzalez, J.P., Mazzucchelli, M.L., Angel, R.J., Alvaro, M., 2021. Elastic Geobarometry for Anisotropic Inclusions in Anisotropic Host Minerals: Quartz-in-Zircon. Journal of Geophysical Research: Solid Earth 126.
Gonzalez, J.P., Thomas, J.B., Baldwin, S.L., Alvaro, M., 2019. Quartz-in-garnet and Ti-in-quartz thermobarometry: Methodology and first application to a quartzofeldspathic gneiss from eastern Papua New Guinea. J. Metamorph. Geol. 37, 1193–1208.
Grüneisen, E., 1926. Zustand des festen Körpers. Handbuch der Physik 1, 1–52.
Harvey, K.M., Penniston-Dorland, S.C., Kohn, M.J., Piccoli, P.M., 2020. Assessing P-T variability in mélange blocks from the Catalina Schist: is there differential movement at the subduction interface? J. Metamorph. Geol. 39, 271–295.
Howell, D., Wood, I.G., Dobson, D.P., Jones, A.P., Nasdala, L., Harris, J.W., 2010.

Quantifying strain birefringence halos around inclusions in diamond. Contrib. Mineral. Petrol. 160, 705–717.
Johnson, T.A., Cottle, J.M., Larson, K.P., 2020. Delineation of multiple metamorphic events in the Himalayan Kathmandu complex, Central Nepal. J. Metamorph. Geol. 39, 443–472.
Key, S.W., 1967. Grüneisen tensor for anisotropic materials. J. Appl. Phys. 38, 2923–2928.
Lakshtanov, D.L., Sinogeilin, S.V., Bass, J.D., 2007. High-temperature phase transitions and elasticity of silica polymorphs. Phys. Chem. Miner. 34, 11–22.
Mazzucchelli, M.L., Angel, R.J., Alvaro, M., 2021. EntraPT: an online platform for elastic geothermobarometry. Am. Mineral. 106, 830–837.
Mazzucchelli, M.L., Burnley, P., Angel, R.J., Morganti, S., Domeneghetti, M.C., Nestola, F., Alvaro, M., 2018. Elastic geothermobarometry: Corrections for the geometry of the host-inclusion system. Geology 46, 231–234.
Mazzucchelli, M.L., Reali, A., Morganti, S., Angel, R.J., Alvaro, M., 2019. Elastic geobarometry for anisotropic inclusions in cubic hosts. Lithos 350–351.
Morana, M., Mihailova, B., Angel, R.J., Alvaro, M., 2020. Quartz metastability at high pressure: what new can we learn from polarized raman spectroscopy? Physics and Chemistry of Minerals 47.
Murri, M., Alvaro, M., Angel, R.J., Prencipe, M., Mihailova, B.D., 2019. The effects of non-hydrostatic stress on the structure and properties of alpha-quartz. Phys. Chem. Miner. 46, 487–499.
Murri, M., Mazzucchelli, M.L., Campomenosi, N., Korsakov, A.V., Prencipe, M., Mihailova, B., Scambelluri, M., Angel, R.J., Alvaro, M., 2018. Raman elastic geobarometery for anisotropic mineral inclusions. Am. Mineral. 103, 1869–1872.
Musiyachenko, K.A., Murri, M., Prencipe, M., Angel, R.J., Alvaro, M., 2021. A Grüneisen tensor for rutile and its application to host-inclusion systems. Am. Mineral. 106, 1586–1595.
Nye, J.F., 1957. Physical Properties of Crystals. Oxford University Press, Oxford.
Nye, J.F., 1985. Physical Properties of Crystals: Their Representation by Tensors and Matrices. Oxford University Press.
Pascale, F., Zicovich-Wilson, C.M., Orlando, R., Roetti, C., Ugliengo, P., Dovesi, R., 2005. Vibration frequencies of $Mg_3Al_2Si_3O_{12}$ pyrope. An ab initio study with the CRYSTAL code. J. Phys. Chem. B 109, 6146–6152.
Prencipe, M., Scanavino, I., Nestola, F., Merlini, M., Civalleri, B., Bruno, M., Dovesi, R., 2011. High-pressure thermo-elastic properties of beryl ($Al_4Be_6Si_{12}O_{36}$) from ab initio calculations, and observations about the source of thermal expansion. Phys. Chem. Miner. 38, 223–239.
Rosenfeld, J.L., Chase, A.B., 1961. Pressure and temperature of crystallization from elastic effects around solid inclusion minerals? Am. J. Sci. 259, 519–541.
Salje, E.K.H., Graeme-Barber, A., Carpenter, M.A., Bismayer, U., 1993. Lattice-Parameters, Spontaneous Strain and Phase-Transitions in $Pb_3(PO_4)_2$. Acta Crystallographica Section B-Structural Science 49, 387–392.
Schmidt, C., Ziemann, M.A., 2000. In-situ Raman spectroscopy of quartz: a pressure sensor for hydrothermal diamond-anvil cell experiments at elevated temperatures. Am. Mineral. 85, 1725–1734.
Schrojenstein Lantman, H.W., Scambelluri, M., Gilio, M., Wallis, D., Alvaro, M., 2021. Extensive fluid–rock interaction and pressure solution in a UHP fluid pathway recorded by garnetite, Lago di Cignana, Western Alps. J. Metamorph. Geol. 39, 501–518.
Shapiro, S.M., Axe, J.D., 1972. Raman Scattering from Polar Phonons. Phys. Rev. B 6, 2420–2427.
Stangarone, C., Angel, R.J., Prencipe, M., Campomenosi, N., Mihailova, B., Alvaro, M., 2019. Measurement of strains in zircon inclusions by Raman spectroscopy. Eur. J. Mineral. 31, 685–694.
Thomas, J.B., Spear, F.S., 2018. Experimental study of quartz inclusions in garnet at pressuresup to 3.0 GPa: evaluating validity of the quartz-in-garnet inclusion elastic thermobarometer. Contrib. Mineral. Petrol. 173, 42.
Valenzano, L., Torres, F.J., Doll, K., Pascale, F., Zicovich-Wilson, C.M., Dovesi, R., 2006. Ab initio study of the vibrational spectrum and related properties of crystalline compounds; the case of $CaCO_3$ calcite. Z. Phys. Chem. 220, 893–912.
Zhong, X., Andersen, N.H., Dabrowski, M., Jamtveit, B., 2019. Zircon and Quartz Inclusions in Garnet Used for Complementary Raman Thermobarometry: Application to the Holsnøy Eclogite, Bergen Arcs, Western Norway. Contributions to Mineralogy and Petrology 174.
Ziman, J.M., 1960. Electrons and Phonons: The Theory of Transport Phenomena in Solids. Oxford University Press, Oxford.